

Spatio-temporal impulse responses in channel flow of viscoelastic fluids

Gokul Hariharan, Mihailo R. Jovanović, and Satish Kumar

Abstract—The study of non-modal amplification of distributed body forces in channel flows of viscoelastic fluids has provided useful insight into the mechanisms that may govern the initial stages of transition to elastic turbulence. However, distributed body forces are not easy to implement in experiments and there is a need to examine amplification of localized body forces. In this work, we use the linearized governing equations to examine such amplification in channel flow of viscoelastic fluids. We first identify the wall-normal location at which the impulsive excitations experience the largest amplification and then analyze the kinetic energy of the fluctuations and the resulting flow structures. For a viscoelastic fluid at low Reynolds numbers, the largest amplification occurs for impulses located near the channel wall. Flow structures that evolve from the localized body force at the optimal location stretch out in the streamwise direction in a viscoelastic fluid, unlike a Newtonian fluid in which disturbances merely diffuse in space due to low inertia. For viscoelastic fluids, we observe the development of vortical structures away from the source of impulsive excitation. This feature is less prominent in Newtonian fluids and it may provide a mechanism for triggering the initial stages of transition to elastic turbulence.

I. INTRODUCTION

Dilute polymer solutions can transition to a turbulent-like flow state (elastic turbulence) at low Reynolds numbers [1]. Elastic turbulence has many favourable and unfavourable technological implications. Elastic turbulence has high potential for enhancing mixing [2] and heat transport [3] in microfluidic flows. It can also be used to produce nonlinear effects to build micro-scale control devices like nonlinear flow resistors and flow memory devices like flip-flops analogous to those in electric circuitry [4]. However, elastic turbulence is undesired in certain industrial applications, such as polymer processing and coating flows [5], [6].

Elastic turbulence was thought to have originated from linear instability of curved streamlines; however recent experimental evidence suggests that elastic turbulence can occur in straight-channels as well [7]–[9]. Straight streamlines are linearly stable to small amplitude perturbations [5] and therefore the underlying mechanism for transition to elastic turbulence in straight channel flows remains unclear.

In order to understand the initial stages of transition to elastic turbulence in straight channels, there have been many efforts to examine non-modal amplification of external disturbances [10]–[14]. Non-modal analysis considers the

possibility that disturbances may be amplified at short times even though they may decay at long times, i.e., even if the system is linearly stable. Disturbances that experience linear non-modal amplification can produce finite-amplitude disturbances that may excite non-linear flow states [15]–[19].

Previous work on non-modal analysis of viscoelastic channel flows have shown that external forces that are either stochastic [10], [11], [13] or deterministic [12], [14] experience significant non-modal amplification, and that the amount of amplification increases with an increase in viscoelastic effects. In all cases, streamwise constant flow structures became increasingly prominent with an increase in viscoelastic effects.

Most previous analysis considered distributed body forces owing to their analytical tractability. Distributed body forces are nonetheless hard to configure in experiments. Even if a method is devised to induce a well-configured distributed body force in an experiment, it is still difficult to segregate the different stages that lead to elastic turbulence, and to specifically discriminate between linear and nonlinear effects. In contrast, localized body forces can be readily approximated in experiments and in numerical analysis. Furthermore, flow transition due to a localized point force can be analyzed systematically in experiments to provide clear insight into the different stages towards transition to turbulence [20]–[22]. From the point of view of analysis, results from a localized point force is equivalent to examining the impulse response of the system.

This paper is organized as follows. In Section II we present governing equations for the channel flow of viscoelastic fluids. In Section III we describe the numerical methods used in this work. In Section IV we discuss methods used to quantify the amount of kinetic energy of velocity fluctuations. The kinetic energy of velocity fluctuations is used to characterize the degree of non-modal amplification. In Section V we identify the optimal location to induce the localized body force. The impulse at the optimal location produces the largest amplification of the kinetic energy of velocity fluctuations. In Section VI we present flow structures that arise from exciting the flow at the optimal location.

II. PROBLEM FORMULATION

We consider pressure-driven plane Poiseuille flow of a viscoelastic fluid with relaxation time λ and density ρ . The flow geometry and coordinate system are shown in Fig. 1. Length is scaled with the half-channel width h , velocity with the maximum velocity in the channel U_0 , and time with h/U_0 . Pressure is scaled with $\eta_T U_0/h$, where $\eta_T = \eta_p + \eta_s$ is the total shear viscosity with η_p and η_s denoting the polymer

Supported in part by the National Science Foundation under award CBET-1510654. The Minnesota Supercomputing Institute (MSI) at the University of Minnesota is gratefully acknowledged for providing computing resources.

G. Hariharan and S. Kumar are with the Department of Chemical Engineering and Materials Science, University of Minnesota, Minneapolis, MN 55455, USA. M. R. Jovanović is with the Ming Hsieh Department of Electrical Engineering, Los Angeles, CA 90089, USA. E-mails: harih020@umn.edu, mihailo@usc.edu, kumar030@umn.edu

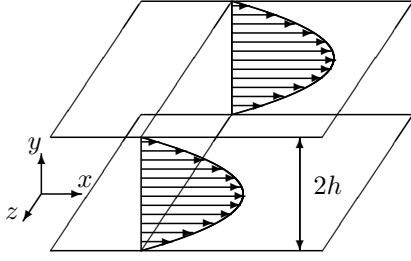


Fig. 1: Flow geometry showing the steady-state velocity profile for plane Poiseuille flow.

and solvent contributions to η_T . Polymer stresses are scaled with $\eta_p U_0/h$.

This scaling leads to three non-dimensional groups: the viscosity ratio, $\beta = \eta_s/(\eta_p + \eta_s)$, the Weissenberg number, $We = \lambda U_0/h$, and the Reynolds number, $Re = h\rho U_0/\eta_T$. The viscosity ratio provides a measure of the solvent contribution to the shear viscosity, the Weissenberg number gives the ratio of the relaxation time of the polymer to the characteristic flow time, h/U_0 , and the Reynolds number is the ratio of the inertial forces to viscous forces.

The dimensionless momentum and mass conservation equations are

$$Re(\partial_t \mathbf{V} + \mathbf{V} \cdot \nabla \mathbf{V}) = -\nabla P + \beta \nabla^2 \mathbf{V} + (1 - \beta) \nabla \cdot \mathbf{T}, \quad (1a)$$

$$\nabla \cdot \mathbf{V} = 0, \quad (1b)$$

where \mathbf{V} is the velocity vector, P is the pressure, and \mathbf{T} is the polymer contribution to stress tensor. The polymer contribution to the stress tensor is modeled using the finitely extensible nonlinear elastic Chilcott Rallison (FENE-CR) constitutive equation [23]. The Oldroyd-B and FENE type constitutive equations come from a statistical averaging of forces on polymer molecules, where each polymer molecule is modeled as binary beads connected by an elastic spring [24], [25]. The Oldroyd-B model assumes that the beads are connected by a linear spring. The linear spring allows for an unrealistic infinite extensibility of polymer molecules. The FENE model corrects this assumption by using a finitely extensible nonlinear spring instead of a linear spring. The FENE-CR model exhibits a constant shear viscosity in addition to accounting for finite extensibility of the polymer molecules. This isolates the influence of fluid elasticity from a mix of elastic and shear thinning effects.

The conformation tensor is the mean of the dyadic product of the end-to-end vector of the finitely extensible dumbbell that is the basis of the FENE-CR model. The polymer stress tensor \mathbf{T} is related to the conformation tensor \mathbf{R} by

$$\partial_t \mathbf{R} + \mathbf{V} \cdot \nabla \mathbf{R} - \mathbf{R} \cdot \nabla \mathbf{V} - (\mathbf{R} \cdot \nabla \mathbf{V})^T = -\mathbf{T}, \quad (1c)$$

$$\frac{f}{We}(\mathbf{R} - \mathbf{I}) = \mathbf{T}, \quad (1d)$$

where \mathbf{I} is the identity tensor and f quantifies the nonlinear

spring interaction,

$$f = \frac{L^2 - 3}{L^2 - \text{trace}(\mathbf{R})}. \quad (1e)$$

We note that \mathbf{R} and L^2 are scaled with kT/c , and k , T , and c are the Boltzmann constant, absolute temperature, and spring constant of the dumbbells, respectively. As $L \rightarrow \infty$, the FENE-CR model simplifies to the Oldroyd-B model. Furthermore, as $\beta \rightarrow 1$ or as $We \rightarrow 0$ the system reduces to the Navier-Stokes equations.

The steady-state solution of system (1) is determined by

$$\bar{\mathbf{V}} = [\bar{U}(y) \quad 0 \quad 0]^T, \quad (2a)$$

$$\bar{\mathbf{R}} = \begin{bmatrix} 1 + 2(We \bar{U}'(y)/\bar{f})^2 & We \bar{U}'(y)/\bar{f} & 0 \\ We \bar{U}'(y)/\bar{f} & 1 & 0 \\ 0 & 0 & 1 \end{bmatrix}, \quad (2b)$$

where

$$\bar{U}(y) = 1 - y^2, \quad \bar{L}^2 = L^2 - 3, \quad (2c)$$

$$\bar{f} = \frac{1}{2} \left(1 + \sqrt{1 + 8 \left(\frac{We \bar{U}'(y)}{\bar{L}} \right)^2} \right). \quad (2d)$$

The steady-state velocity has the same parabolic profile as a Newtonian fluid because of the absence of shear-thinning effects in the FENE-CR constitutive equation. We note, however, that there is a first normal stress difference in the FENE-CR model.

Equations Governing Fluctuations about the Mean Flow

The linearized equations that govern the evolution of fluctuations about the steady-state (2) are given by

$$Re \partial_t \mathbf{v} = -\nabla p + (1 - \beta) \nabla \cdot \boldsymbol{\tau} + \beta \nabla^2 \mathbf{v} - Re(\bar{\mathbf{V}} \cdot \nabla \mathbf{v} + \mathbf{v} \cdot \nabla \bar{\mathbf{V}}) + \mathbf{d}, \quad (3a)$$

$$\nabla \cdot \mathbf{v} = 0, \quad (3b)$$

$$\partial_t \mathbf{r} = \mathbf{r} \cdot \nabla \bar{\mathbf{V}} + \bar{\mathbf{R}} \cdot \nabla \mathbf{v} + (\mathbf{r} \cdot \nabla \bar{\mathbf{V}})^T + (\bar{\mathbf{R}} \cdot \nabla \mathbf{v})^T - \mathbf{v} \cdot \nabla \bar{\mathbf{R}} - \bar{\mathbf{V}} \cdot \nabla \mathbf{r} - \boldsymbol{\tau}, \quad (3c)$$

$$\boldsymbol{\tau} = \frac{\bar{f}}{We} \left(\mathbf{r} + \frac{\bar{f}(\bar{\mathbf{R}} - \mathbf{I})}{\bar{L}^2} \text{trace}(\mathbf{r}) \right). \quad (3d)$$

Here, \mathbf{v} , p , \mathbf{r} , and $\boldsymbol{\tau}$ denote velocity, pressure, conformation tensor, and stress tensor fluctuations about their respective base profiles, $\bar{\mathbf{V}}$, \bar{P} , $\bar{\mathbf{R}}$, and $\bar{\mathbf{T}}$. We denote the components of the velocity fluctuation vector by $\mathbf{v} = [u \ v \ w]^T$, where u , v , and w represent the streamwise (x), wall-normal (y), and spanwise (z) velocities, respectively.

From (1d) and (3d) it may appear that the stress tensor, \mathbf{T} , and its fluctuation, $\boldsymbol{\tau}$, can become infinite when $We = 0$. However, this is not the case. By eliminating \mathbf{R} and \mathbf{r} from (1) and (3), it can be shown that the stress tensor reverts to that of a Newtonian fluid at $We = 0$. It is essential for any valid polymeric constitutive equation that the system simplifies to that of a Newtonian fluid as $We \rightarrow 0$ [24], [25].

The body forcing \mathbf{d} in (3a) is used to excite flow fluctuations. In this work, we use an impulsive body force,

$$\mathbf{d}(x, y, z, t) = \delta(x, y, z, t) \mathbf{e}_i, \quad (4)$$

where, \mathbf{e}_i is a unit vector in the i^{th} coordinate direction and $\delta(x, y, z, t)$ is the Dirac delta function in space and time.

System (3) can be recast into the state-space representation by eliminating pressure and expressing the velocity fluctuations in terms of wall-normal velocity v and vorticity $\eta := \partial_z u - \partial_x w$. This is done by taking the divergence of (3a) to get an explicit expression for p . Substituting this expression for p to (3a) yields the equation for the wall-normal velocity and the equation for η is determined by the y -component of the curl of (3a). Finally, the stress tensor can be eliminated in favor of the conformation tensor using relations (3c) and (3d).

After the above algebraic manipulations, and after taking a Fourier transform in the x - and z -directions, we obtain the evolution form for the linearized equations parametrized by wavenumbers $\boldsymbol{\kappa} = (k_x, k_z)$,

$$\begin{aligned} \partial_t \boldsymbol{\psi}(y, \boldsymbol{\kappa}, t) &= \mathbf{A}(\boldsymbol{\kappa}) \boldsymbol{\psi}(y, \boldsymbol{\kappa}, t) + \mathbf{B}(\boldsymbol{\kappa}) \mathbf{d}(y, \boldsymbol{\kappa}, t), \\ \boldsymbol{\phi}(y, \boldsymbol{\kappa}, t) &= \mathbf{C}(\boldsymbol{\kappa}) \boldsymbol{\psi}(y, \boldsymbol{\kappa}, t), \end{aligned} \quad (5)$$

where the state vector $\boldsymbol{\psi}$ and output vector $\boldsymbol{\phi}$ are given by

$$\begin{aligned} \boldsymbol{\psi} &= [\mathbf{r}^T \ v \ \eta]^T, \\ \boldsymbol{\phi} &= [u \ v \ w]^T, \end{aligned}$$

and \mathbf{r} is the vector of the six (symmetric) components of the conformation tensor. The operators $\mathbf{A}(\boldsymbol{\kappa})$, $\mathbf{B}(\boldsymbol{\kappa})$, and $\mathbf{C}(\boldsymbol{\kappa})$ in (5) will be detailed elsewhere due to space constraints.

III. NUMERICAL METHOD

The y -dependence is numerically approximated using a Chebyshev collocation technique with N collocation points to reduce (5) to a system of ordinary differential equations (ODEs) in time. Calculations are carried out using a Matlab Differentiation Matrix Suite of Weidmann and Reddy [26]. This discretization necessitates a finite approximation of the Dirac delta function in the wall-normal direction. We use the approximation

$$\delta_0(y) = \frac{1}{2\sqrt{\pi\epsilon}} e^{-\frac{(y-y_0)^2}{4\epsilon}}, \quad \epsilon > 0. \quad (6a)$$

In this work, we set $\epsilon = 1/2000$. We found that this value is sufficiently small to represent an impulse as the results do not change significantly on further reducing ϵ . The impulse response of the viscoelastic system is studied for different values of y_0 to identify the optimal location. The forcing term in the evolution model (5) is then given by,

$$\mathbf{B}(\boldsymbol{\kappa}) \mathbf{d}(y, \boldsymbol{\kappa}, t) = \mathbf{F}_i(y, \boldsymbol{\kappa}) \delta(t), \quad (6b)$$

where

$$\mathbf{F}_i(y, \boldsymbol{\kappa}) = \mathbf{B}(\boldsymbol{\kappa}) \delta_0(y) \mathbf{e}_i. \quad (6c)$$

The finite-dimensional approximation to (5) is given by

$$\begin{aligned} \partial_t \boldsymbol{\psi}(\boldsymbol{\kappa}, t) &= \mathbf{A}(\boldsymbol{\kappa}) \boldsymbol{\psi}(\boldsymbol{\kappa}, t) + \mathbf{F}_i(\boldsymbol{\kappa}) \delta(t), \\ \boldsymbol{\phi}(\boldsymbol{\kappa}, t) &= \mathbf{C}(\boldsymbol{\kappa}) \boldsymbol{\psi}(\boldsymbol{\kappa}, t), \end{aligned} \quad (7)$$

where $\boldsymbol{\psi}(\boldsymbol{\kappa}, t)$ and $\boldsymbol{\phi}(\boldsymbol{\kappa}, t)$ are complex-valued vectors with $8N$ and $3N$ entries, respectively, $\mathbf{A}(\boldsymbol{\kappa})$, $\mathbf{C}(\boldsymbol{\kappa})$ are finite-dimensional approximations of the corresponding operators in (5), and $\mathbf{F}_i(\boldsymbol{\kappa})$ is the discrete approximation to $\mathbf{F}_i(y, \boldsymbol{\kappa})$ in (6b).

The solution to (7) with zero initial conditions arising from the impulsive excitation in the i^{th} coordinate direction is given by [27],

$$\begin{aligned} \boldsymbol{\phi}_i(\boldsymbol{\kappa}, t) &= \mathbf{C}(\boldsymbol{\kappa}) \int_0^t e^{\mathbf{A}(\boldsymbol{\kappa})(t-s)} \mathbf{F}_i(\boldsymbol{\kappa}) \delta(s) ds \\ &= \mathbf{C}(\boldsymbol{\kappa}) e^{\mathbf{A}(\boldsymbol{\kappa})t} \mathbf{F}_i(\boldsymbol{\kappa}). \end{aligned} \quad (8)$$

Thus, the impulse response is directly obtained from the matrix exponential at a given time and the inverse Fourier transform in wall-parallel directions yields solution in physical space.

IV. KINETIC ENERGY OF VELOCITY FLUCTUATIONS

The integral of kinetic energy of velocity fluctuations in the wall-normal direction can be evaluated by using a weighted inner product of the output with itself

$$\begin{aligned} \left[\int_{-1}^1 |u_i|^2 + |v_i|^2 + |w_i|^2 dy \right] (\boldsymbol{\kappa}, t) &= [\boldsymbol{\phi}_i^H \mathbf{I}_w \boldsymbol{\phi}_i] (\boldsymbol{\kappa}, t) \\ &:= E_i(\boldsymbol{\kappa}, t), \end{aligned} \quad (9)$$

where $(\cdot)^H$ represents the complex conjugate transpose, and \mathbf{I}_w is a diagonal matrix of the appropriate integration weights for the Chebyshev collocation points. We recall that the subscript i denotes the input direction of the impulsive excitation (see (4)).

We further define the numerical approximation to the integral of the kinetic energy over the wall-normal direction and over all time as

$$\left[\int_{t=0}^{\infty} \int_{y=-1}^1 |u_i|^2 + |v_i|^2 + |w_i|^2 dy dt \right] (\boldsymbol{\kappa}) := \bar{E}_i(\boldsymbol{\kappa}). \quad (10a)$$

We note that for stable systems, it is not necessary to explicitly integrate over all time to evaluate $\bar{E}_i(\boldsymbol{\kappa})$. They can be estimated using solutions to the operator Lyapunov equations [18],

$$\mathbf{A}(\boldsymbol{\kappa}) \mathbf{X}_i(\boldsymbol{\kappa}) + \mathbf{X}_i(\boldsymbol{\kappa}) \mathbf{A}^\dagger(\boldsymbol{\kappa}) = -\mathbf{F}_i(\boldsymbol{\kappa}) \mathbf{F}_i^\dagger(\boldsymbol{\kappa}), \quad (10b)$$

where $(\cdot)^\dagger$ represents the finite-dimensional approximations to the adjoints of operators that appear in (5). Adjoints are defined with respect to a weighted inner product that determines the kinetic energy of the system [18], [28]. Solution to (10b) yields \mathbf{X}_i and the kinetic energy can be determined as

$$\bar{E}_i(\boldsymbol{\kappa}) = \text{trace}(\mathbf{X}_i(\boldsymbol{\kappa}) \mathbf{C}^\dagger(\boldsymbol{\kappa}) \mathbf{C}(\boldsymbol{\kappa})). \quad (10c)$$

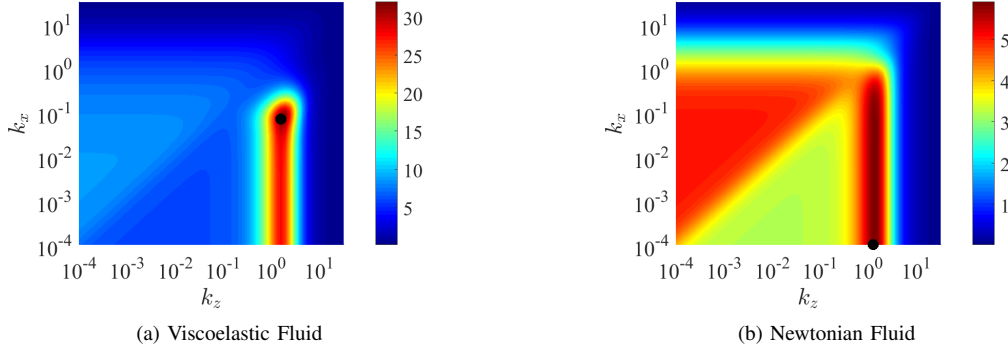


Fig. 2: Kinetic energy integrated in the wall-normal direction and time, with an impulse in the spanwise direction, calculated using (10). We consider a (a) viscoelastic fluid and a (b) Newtonian fluid. Parameters used for the viscoelastic fluid are $We = 50$, $L = 100$ and $\beta = 0.5$. The maximum value of the kinetic energy is indicated by the black dots.

V. SENSITIVITY TO THE LOCATION OF THE IMPULSE

The location of the impulse in the (x, z) -plane is immaterial because the x - and z -directions are translationally invariant. However, the sensitivity of the flow may vary with the choice of the location of the impulse in the wall-normal direction. We next examine how the sensitivity of a viscoelastic channel flow changes with the wall-normal location of impulsive forcing.

Due to the symmetry of plane Poiseuille flow, we only consider the lower half of the channel. We first calculate the kinetic energy averaged over the wall-normal direction and time (using relation (10)) with respect to k_x and k_z for different values of y_0 . For example, Fig. 2 shows the kinetic energy for an impulsive excitation in the spanwise direction for $y_0 = -0.75$, $Re = 50$ for a viscoelastic fluid (Fig. 2a) and a Newtonian fluid (Fig. 2b). The maximum value of the kinetic energy over all values of k_x and k_z is marked by the black dots in Fig. 2. In Fig. 3, we examine how these maximum values depend on the location of the impulse, y_0 .

We restrict ourselves to results pertaining to the spanwise impulsive excitation as we found the largest energy amplification for disturbances excited in the spanwise direction. A more detailed analysis of impulsive excitations in other directions will be reported elsewhere.

We see in Fig. 3 that the introduction of viscoelasticity increases the kinetic energy of velocity fluctuations for an impulsive excitation at any location. Larger amplification of disturbances in viscoelastic fluids indicates their greater sensitivity at relatively low values of the Reynolds number, and this may be related to observed transition at low Reynolds numbers. The largest discrepancy between corresponding kinetic energies occurs for the impulse in the spanwise direction at a location $y_0 = -0.75$, whose corresponding energies are plotted in Fig. 2. We see from the colorbars in Fig. 2 that at the location with largest amplification, the viscoelastic fluid amplifies disturbances six times more when compared to the Newtonian fluid.

We note that for $y_0 = -0.75$ the maximum value of the kinetic energy occurs at $(k_x \approx 10^{-1}, k_z \approx 10^0)$ in Fig. 2a,

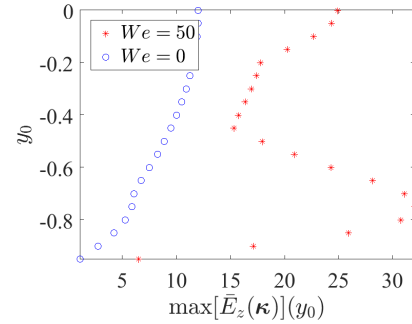


Fig. 3: Maximum energy induced by the impulse as a function of y_0 . Parameters used for the viscoelastic fluid are $We = 50$, $L = 100$ and $\beta = 0.5$. The Newtonian fluid corresponds to $We = 0$.

and at $(k_x \approx 10^{-4}, k_z \approx 10^0)$ in Fig. 2b. These values change as we change y_0 .

VI. FLOW STRUCTURES IN PHYSICAL SPACE

Having analyzed energy, we now show flow structures that evolve by inducing an impulsive excitation in the spanwise direction at the optimal location of the viscoelastic fluid. Flow structures in physical space provide a view into patterns that result from a localized point force, and can suggest potential mechanisms that govern the initial stages of transition to turbulence at low Reynolds numbers. Flow structures presented here are obtained by the spectral method described in Section III. Time series of flow structures are therefore direct numerical simulations on the linearized FENE-CR fluid with an impulsive point force. We note that we do not step in time; rather, we exploit linearity to directly obtain flow structures at a given time using the matrix exponential (see (8)).

Fig. 4 shows three-dimensional isosurface plots of the streamwise velocity with an impulsive excitation in the spanwise direction at $y_0 = -0.75$. We analyze the streamwise velocity as we found that the streamwise fluctuation velocity

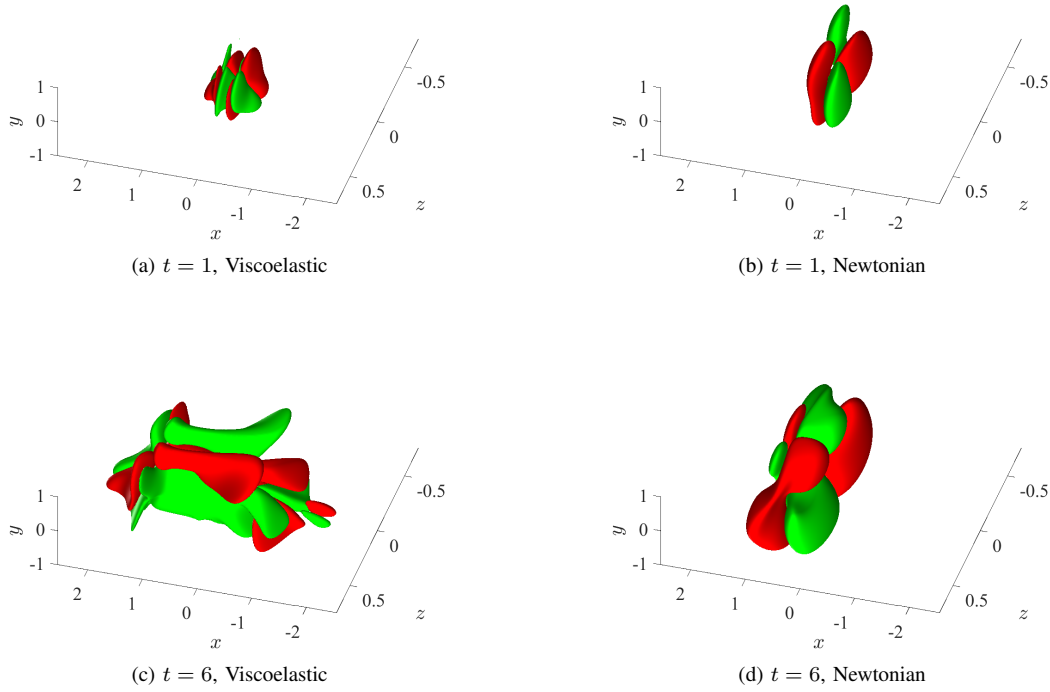


Fig. 4: Isosurface plots of the streamwise velocity at $\pm u_{z,max}/10$ at $Re = 50$. Red denotes regions of high velocity and green denotes regions of low velocity. Panels correspond to a viscoelastic fluid at (a) 1, and (c) 6 time units, and a Newtonian fluid at (b) 1 and (d) 6 time units, with parameters $L = 100$, $\beta = 0.5$ and $We = 50$ for the viscoelastic fluid.

is most amplified when compared to the wall-normal and spanwise fluctuation velocities.

Fig. 4a and Fig. 4c show the time-evolution for a viscoelastic fluid, and Fig. 4b and Fig. 4d illustrate the time-evolution for a Newtonian fluid. We noticed from Fig. 2a that the viscoelastic fluid produces more oblique wave structures ($k_x \approx 10^{-1}$, $k_z \approx 10^0$) when compared to the Newtonian fluid in Fig. 2b in which streamwise-constant structures are most prominent ($k_x \approx 10^{-4}$, $k_z \approx 10^0$). Consistently, we see in Fig. 4c that at early times, the disturbance in the viscoelastic fluid is more oblique, showing a wavy nature in all three directions. At later times (Fig. 4c) the wave packet stretches out in the streamwise direction and is also found to spread across the channel in the wall-normal (y) direction. In contrast, the impulse-induced wave packet in the Newtonian fluid merely diffuses in space slowly (by observing the scales in the x -axis) with a slight amount of translation in the streamwise direction.

Flow structures can be further analyzed by looking at three-dimensional streamtubes of the fluctuation velocity vector. Fig. 5 shows three-dimensional streamtubes that originate from the plane $y = 0.5$ for a viscoelastic fluid and a Newtonian fluid.

Fig. 5b and Fig. 5d show the top and isometric views of streamtubes for a Newtonian fluid, and Fig. 5a and Fig. 5c show the top and isometric views for a viscoelastic fluid at

$t = 6$. We see in Fig. 5a and Fig. 5c that the viscoelastic fluid generates two pairs of counter-rotating vortices at $x = \pm 1$ that spread out in the wall-normal direction with an oblique inclination.

In contrast, we do not find significant evolution of vortical structures in the Newtonian fluid (in Fig. 5b and Fig. 5d), in fact, streamtubes for the Newtonian fluid at $t = 6$ (Fig. 5b and Fig. 5d) were found to be almost as they were at initial times (Figures for initial times is not shown here). The time-evolution of the vortical structures observed here is distinct to the viscoelastic fluid. Vortex breakdown is a well-known mechanism for transition to turbulence in Newtonian fluids at high Reynolds numbers [29]. Analyzing the existence of a breakdown and corresponding transition cannot be captured within the linearized dynamics, and would need consideration of nonlinear effects. However, within the linearized dynamics, we find the development of vortical structures that may be related to the initial stages of transition to elastic turbulence.

REFERENCES

- [1] A. Groisman and V. Steinberg, “Elastic turbulence in a polymer solution flow,” *Nature*, vol. 405, no. 6782, pp. 53–55, 2000.
- [2] T. Burghel, E. Segre, I. Bar-Joseph, A. Groisman, and V. Steinberg, “Chaotic flow and efficient mixing in a microchannel with a polymer solution,” *Phys. Rev. E*, vol. 69, p. 066305, 2004.
- [3] D. Copeland, C. Ren, M. Su, and P. Ligrani, “Elastic turbulence influences and convective heat transfer within a miniature viscous disk pump,” *Int. J. Heat Mass Transfer*, vol. 108, pp. 1764–1774, 2017.

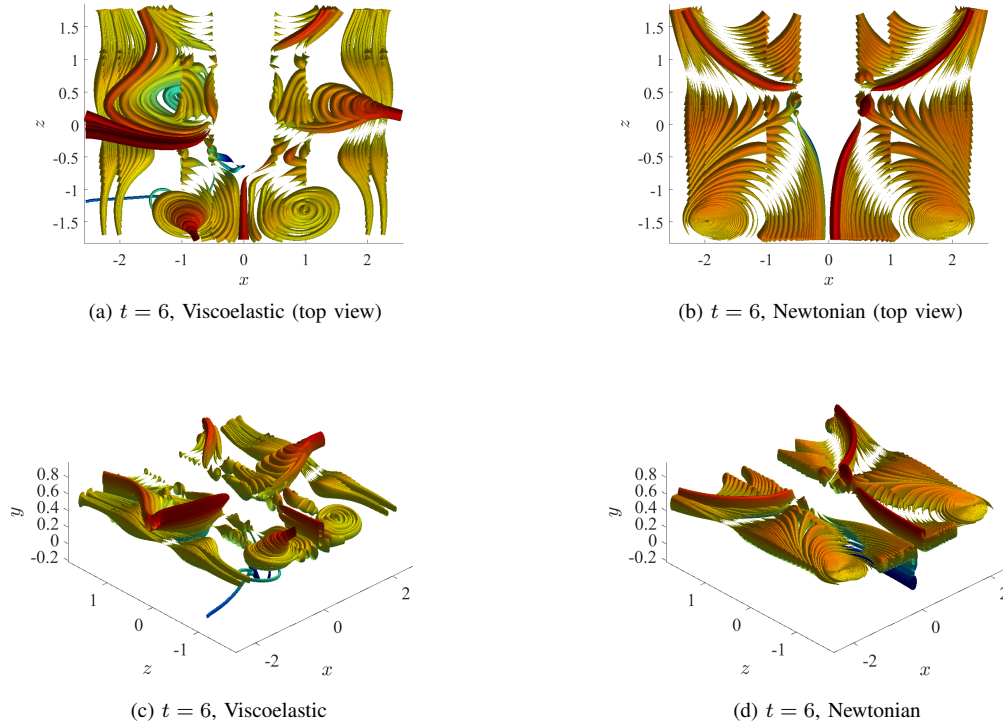


Fig. 5: Three-dimensional streamtubes of the fluctuation velocity vector that originate from the plane $y = 0.5$ at $Re = 50$ with a spanwise impulsive excitation at $y_0 = -0.75$. Figure show (a) top view and (c) isometric view for a viscoelastic fluid and (b) top view and (d) isometric view for a Newtonian fluid at $t = 6$. Parameters used for the viscoelastic fluid are $L = 100$, $\beta = 0.5$ and $We = 50$.

- [4] A. Groisman, M. Enzelberger, and S. R. Quake, "Microfluidic memory and control devices," *Science*, vol. 300, no. 5621, pp. 955–958, 2003.
- [5] R. G. Larson, "Instabilities in viscoelastic flows," *Rheol. Acta*, vol. 31, no. 3, pp. 213–263, 1992.
- [6] A. N. Morozov and W. van Saarloos, "Subcritical finite-amplitude solutions for plane Couette flow of viscoelastic fluids," *Phys. Rev. Lett.*, vol. 95, p. 024501, 2005.
- [7] L. Pan, A. Morozov, C. Wagner, and P. Arratia, "Nonlinear elastic instability in channel flows at low Reynolds numbers," *Phys. Rev. Lett.*, vol. 110, no. 17, p. 174502, 2013.
- [8] B. Qin and P. E. Arratia, "Characterizing elastic turbulence in channel flows at low Reynolds number," *Phys. Rev. Fluids*, vol. 2, p. 083302, 2017.
- [9] D. Bonn, F. Ingremeau, Y. Amarouchene, and H. Kellay, "Large velocity fluctuations in small-Reynolds-number pipe flow of polymer solutions," *Phys. Rev. E*, vol. 84, p. 045301, 2011.
- [10] N. Hoda, M. R. Jovanović, and S. Kumar, "Energy amplification in channel flows of viscoelastic fluids," *J. Fluid Mech.*, vol. 601, pp. 407–424, April 2008.
- [11] N. Hoda, M. R. Jovanović, and S. Kumar, "Frequency responses of streamwise-constant perturbations in channel flows of Oldroyd-B fluids," *J. Fluid Mech.*, vol. 625, pp. 411–434, April 2009.
- [12] M. R. Jovanović and S. Kumar, "Transient growth without inertia," *Phys. Fluids*, vol. 22, no. 2, p. 023101 (19 pages), February 2010.
- [13] M. R. Jovanović and S. Kumar, "Nonmodal amplification of stochastic disturbances in strongly elastic channel flows," *J. Non-Newtonian Fluid Mech.*, vol. 166, no. 14–15, pp. 755–778, August 2011.
- [14] B. K. Lieu, M. R. Jovanović, and S. Kumar, "Worst-case amplification of disturbances in inertialess Couette flow of viscoelastic fluids," *J. Fluid Mech.*, vol. 723, pp. 232–263, May 2013.
- [15] M. R. Jovanović and B. Bamieh, "The spatio-temporal impulse response of the linearized Navier-Stokes equations," in *Proceedings of the 2001 American Control Conference*, 2001, pp. 1948–1953.
- [16] M. R. Jovanović and B. Bamieh, "Modelling flow statistics using the linearized Navier-Stokes equations," in *Proceedings of the 40th IEEE Conference on Decision and Control*, 2001, pp. 4944–4949.
- [17] M. R. Jovanović, "Modeling, analysis, and control of spatially distributed systems," Ph.D. dissertation, University of California, Santa Barbara, 2004.
- [18] M. R. Jovanović and B. Bamieh, "Componentwise energy amplification in channel flows," *J. Fluid Mech.*, vol. 534, pp. 145–183, July 2005.
- [19] P. J. Schmid, "Nonmodal stability theory," *Annu. Rev. Fluid Mech.*, vol. 39, pp. 129–162, 2007.
- [20] B. G. Klingmann, "On transition due to three-dimensional disturbances in plane Poiseuille flow," *J. Fluid Mech.*, vol. 240, pp. 167–195, 1992.
- [21] D. R. Carlson, S. E. Widnall, and M. F. Peeters, "A flow-visualization study of transition in plane Poiseuille flow," *J. Fluid Mech.*, vol. 121, pp. 487–505, 1982.
- [22] G. Lemoult, K. Gumowski, J.-L. Aider, and J. E. Wesfreid, "Turbulent spots in channel flow: An experimental study," *Eur. Phys. J. E*, vol. 37, no. 4, p. 25, 2014.
- [23] M. Chilcott and J. M. Rallison, "Creeping flow of dilute polymer solutions past cylinders and spheres," *J. Non-Newtonian Fluid Mech.*, vol. 29, pp. 381–432, 1988.
- [24] R. G. Larson, *The structure and rheology of complex fluids*. Oxford University Press, 1998.
- [25] R. B. Bird, C. F. Curtiss, R. C. Armstrong, and O. Hassager, *Dynamics of Polymeric Liquids, Vol. 2, Kinetic Theory*. John Wiley & Sons, 1987.
- [26] J. A. Weideman and S. C. Reddy, "A MATLAB differentiation matrix suite," *ACM TOMS*, vol. 26, no. 4, pp. 465–519, 2000.
- [27] J. P. Hespanha, *Linear systems theory*. Princeton University Press, 2009.
- [28] K. M. Butler and B. F. Farrell, "Three-dimensional optimal perturbations in viscous shear flow," *Phys. Fluids A*, vol. 4, no. 8, pp. 1637–1650, 1992.
- [29] M. G. Hall, "Vortex breakdown," *Annu. Rev. Fluid Mech.*, vol. 4, no. 1, pp. 195–218, 1972.